ACS NANO

www.acsnano.org

ARTICLE

MXene-Based Mixed Conductor Interphase for Dendrite-Free Flexible Al Organic Battery

Long Yao, Shunlong Ju, Tian Xu, Wenbin Wang, and Xuebin Yu*

Cite This: *ACS Nano* 2023, 17, 25027−25036

Read Online

ACCESS | Metrics & More | Article Recommendations | Supporting Information

ABSTRACT: **Al batteries are promising post-Li battery technologies for large-scale energy storage applications owing to their low cost and high theoretical capacity. However, one of the challenges that hinder their development is the unsatisfactory plating/stripping of the Al metal anode. To circumvent this issue, an ultrathin MXene layer is constructed on the surface of Al by in situ chemical reactions at room temperature. The as-prepared flexible MXene film acts like armor to protect the Al-metal by its high ionic conductivity and high mechanical flexibility. The MXene endow the Al anode with a long cyclic life of more than 5000 h at ultrahigh current density of 50 mA cm^{-2} for Al//Al batteries and a retention of 100% over 200 cycles for 355 Wh kg^{-1} PTO//Al batteries. This work provides fresh insights into the formation and regulation of stable electrode−electrolyte interfaces as well as effective strategies for improving Al metal batteries.**

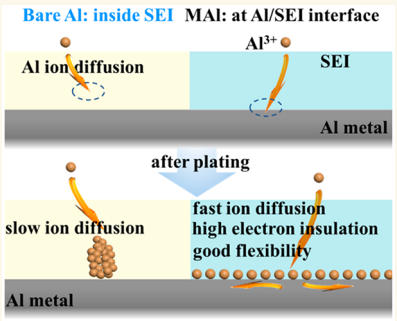

KEYWORDS: *Al batteries, Al metal anode, MXene, dendrite-free, nonaqueous electrolyte*

1. INTRODUCTION

To address rising energy demand, large-scale energy storage solutions that are both sustainable and dependable are urgently needed.[1−3] Despite dominating the current energy storage landscape, it is difficult for lithium-ion batteries to meet large-scale energy storage needs due to intrinsic difficulties such as high cost and lack of lithium resources.[4−6] This conundrum has resulted in the rapid development of alternative battery technology recently, particularly the battery technology that utilize monovalent (Na^+, K^+) or multivalent (Mg^{2+}, Al^{3+}, Ca^{2+}, Zn^{2+}) cations as charge carriers in promising charge storage capacity.[7−12] Among these energy storage technologies, rechargeable aluminum−metal batteries (RABs) have broad prospects as safe transportation power sources and feasible grid level energy storage solutions due to the attractive volume/gravity capacity of aluminum (8056 mAh cm^{-3} and 2981 mAh g^{-1}), low cost, abundant earth resources, and high charge density (Figure S1).[13−15]

In typical aqueous electrolytes, the Al anode struggles with low plating/stripping Coulombic efficiency, low reversibility, a narrow electrochemical stability window, and the development of undesirable passivation products, which cause rapid capacity fading. As a result, the majority of the water-based aluminum metal batteries that have been reported so far can only function at low current densities.[16−18] Ideally, an ionic liquid electrolyte may simplify the plating/stripping of Al metal, thus avoiding the possibility of Al passivation. This is because, thermodynamically, Al is more stable in nonaqueous electrolytes than in aqueous ones. Furthermore, the use of ionic liquid electrolytes can expand the stability window, providing exciting opportunities for the development of high voltage Al batteries.[19] However, these RABs still suffer from inadequate cycling stability in an ionic liquid electrolyte. It was shown that the poor rechargeability is mostly caused by the irreversibility of Al anode due to the formation of aluminum dendrites.[20,21] Moreover, there is a chemical driving force that favors the growth of Al electrodeposits into the glass fiber (SiO_2) membranes separator via an interfacial reaction: $4Al + 3SiO_2 \rightarrow 2Al_2O_3$, which would further increase the possibility of aluminum dendrites piercing the battery separator.[21] Furthermore, Al exhibits a Young's modulus (E) considerably higher than those of Li and Na metals ($E_{Al} \approx 69$ GPa; $E_{Li} \approx 5$ GPa; $E_{Na} \approx 10$ GPa). As a result, the occurrence of separator puncture, which results in cell failure, is more likely occurred in Al than in other alkali metals.[20] Therefore, it is an urgent desire to develop effective strategies to protect the Al anode against undesired dendrites in an ionic liquid electrolyte. So far, only limited studies have focused on unlocking the potential of metallic Al in an ionic liquids system. For example, modifying the Al host materials for ensuring uniform Al plating/stripping is a feasible strategy. Archer and his colleagues pioneered the

Received: August 14, 2023
Revised: November 30, 2023
Accepted: December 4, 2023
Published: December 7, 2023

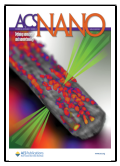

https://doi.org/10.1021/acsnano.3c07611
ACS Nano 2023, 17, 25027−25036

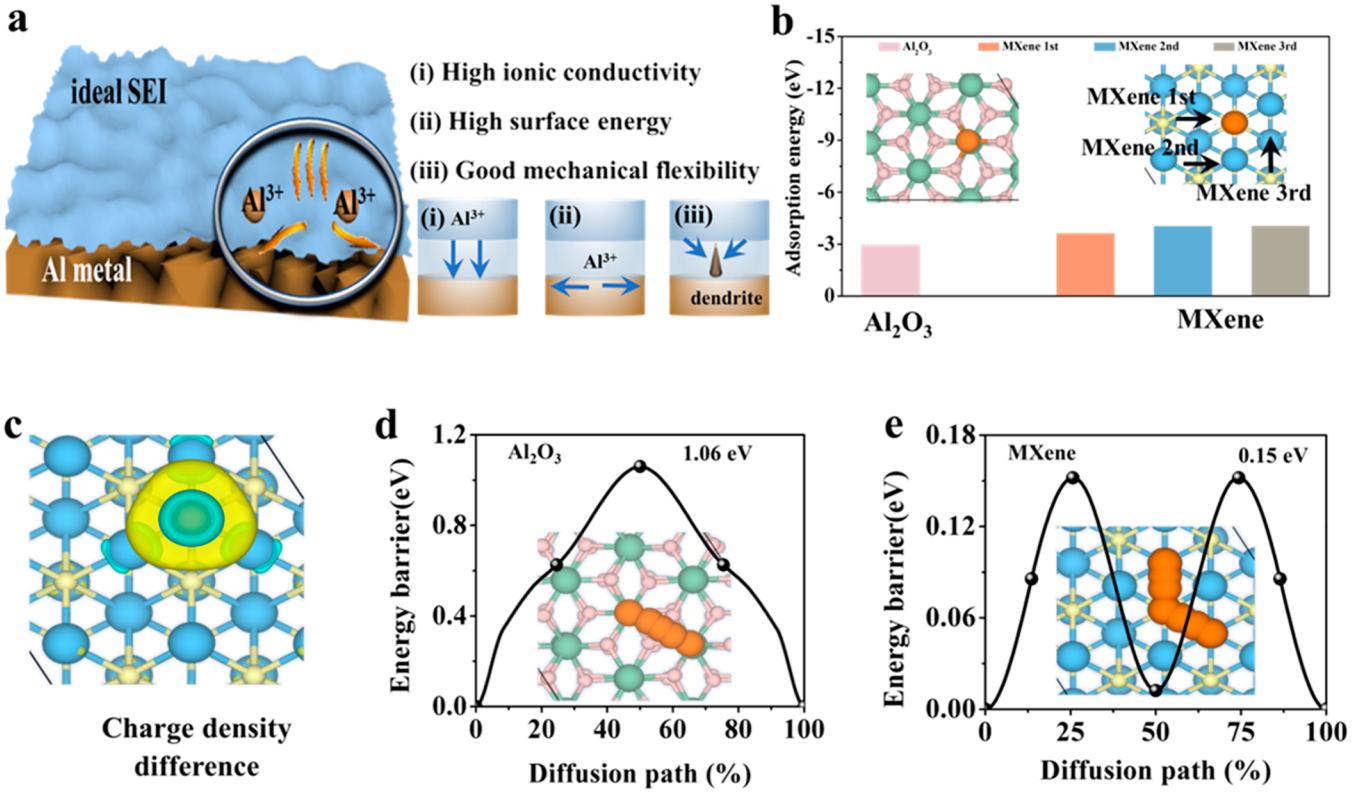

Figure 1. (a) Schematic illustration of an ideal SEI layer. (b) Adsorption sites and the corresponding adsorption energy of Al^{3+} on the MXene and Al_2O_3 surfaces. (c) Charge density differences of Al^{3+} on the surfaces of MXene. The yellow and cyan spheres represent electron accumulation and depletion, respectively. Kinetic energy barriers of Al^{3+} diffusion on the (d) MXene and (e) Al_2O_3 surfaces. The orange spheres represent the diffusion pathways on the surfaces.

use of carbon cloth modified with oxygen-containing functional groups to induce uniform deposition of Al metal and promote stable cycling of Al anodes by Al−O−C bonds.[21] A 3D-structured MXene paper electrode was fabricated to protect Al deposition/dissolution reactions with improved redox kinetics.[22] Au lattice-matching layer can significantly enhance the Al nucleation density, which achieve highly reversible, dendrite-free, durable, and anode-free Al anodes.[23] In addition, designing Al metal anodes with special structures has been proven to be another feasible solution. Yang et al. recommended porous aluminum as the anode. This porous structure provides a uniform ion flow and reduces local current density, effectively enhancing the Al metal anode to maintain cycling stability over a wide range of current densities and area capacities.[20] Another promising technique for regulating the stripping/plating of Al metal is the application of an artificial solid-electrolyte interface (SEI) protective layer on the metal anode. The graphite coating layer can effectively suppress the dendrite growth of Al toward high-performance Al battery with lower overpotential and better cycling stability.[24] Figure 1a demonstrates that Al metal deposition may happen either within the SEI or at the SEI/Al interface, depending upon the diffusion speed of Al^{3+}. Assuming fast ion transport in the SEI, metal aluminum will deposit at the SEI/Al interface, but if not, it may nucleate inside the SEI layer. The latter scenario is particularly problematic at high current densities because isolated Al dendrites within the SEI lose electronic contact with metal Al, leading to inhomogeneous Al deposition. Moreover, these Al dendrites could potentially break the SEI layer, causing battery failure. Consequently, an ideal SEI layer should possess high ionic conductivity to mitigate Al plating within the SEI. Additionally, high mechanical flexibility is crucial for withstanding significant volume changes and preventing dendritic growth at the SEI/Al interfaces.

Herein, to tackle the issue of its inherent irreversibility due to uncontrolled dendritic growth, we designed an MXene-based mixed ionic/electronic conductor interphase layer with adjustable Al^{3+} flux and electric field distribution to improve the Al stripping/plating. The in situ production of MXene interfacial layers will be in close contact with Al anodes via a spontaneously reducing/assembling method, resulting in a homogeneous surface and enhanced stability, which will benefit the fast transport of Al^{3+}. The high mechanical flexibility of 2D MXene films is also crucial to withstand large volume changes and suppress dendritic growth. More importantly, the MXene layer with appropriate electronic conductivity can homogenize the electric field distribution on the electrode surface, which is beneficial for smooth deposition of metal Al on the Al anode surface. As a result, the integration of MXene into the Al anode results in a reduction in voltage hysteresis and exceptional long-term stability with dendrite-free characteristics. Finally, the MXene modified Al metal anode, tested in combination with an organic cathode, pyrene-4,5,9,10-tetraone (PTO), exhibits a long-term cycle stability with a specific capacity of 280 mAh g^{-1} at a voltage of 1.8 V. A practical belt-shaped PTO//MAl battery with an energy density of 355 Wh kg^{-1} has been well demonstrated in wearable electronic devices.

https://doi.org/10.1021/acsnano.3c07611
ACS Nano 2023, 17, 25027−25036

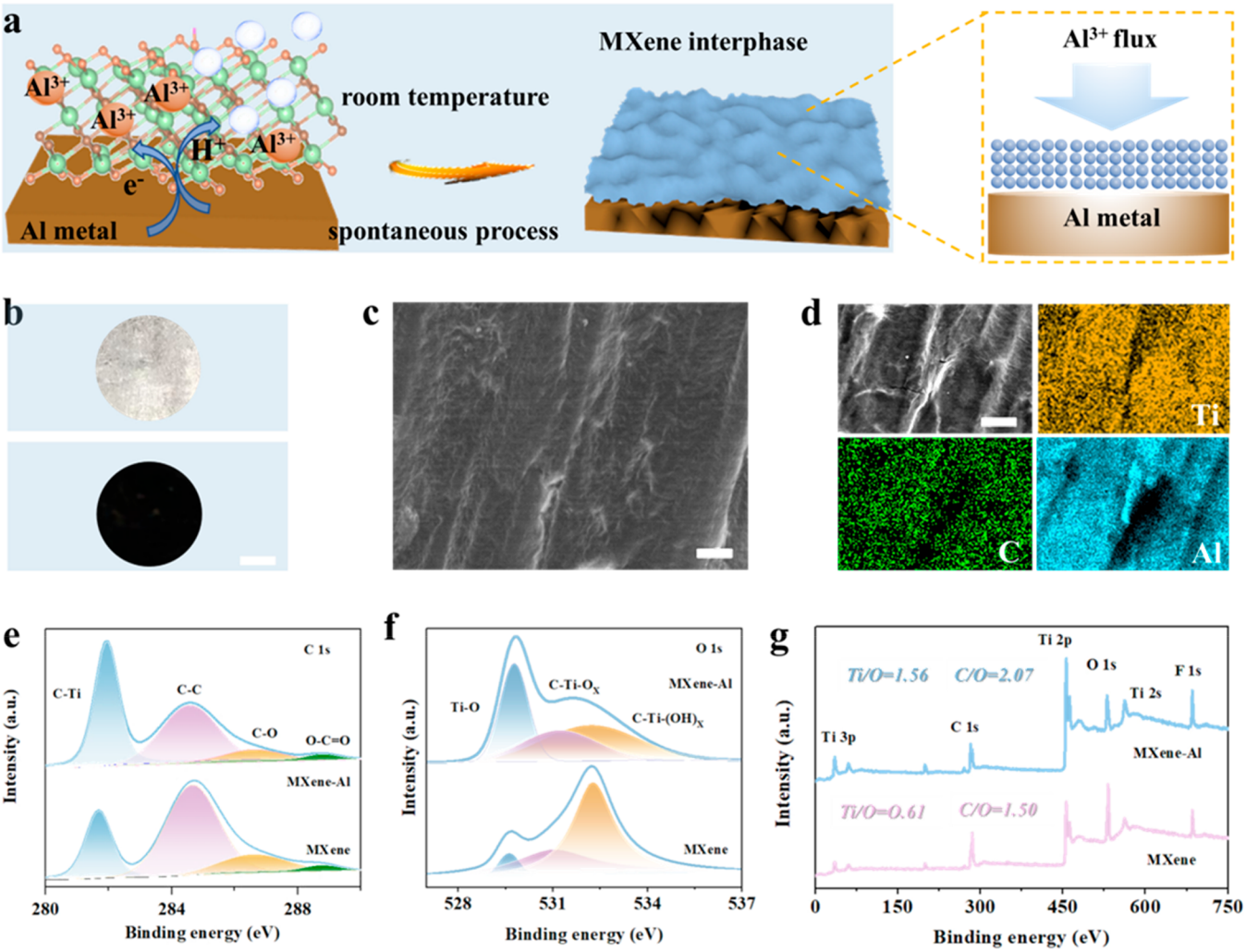

Figure 2. (a) Schematic illustration of the MXene hybrid interphase on Al foil. (b) The optical images of the bare Al film (upper) and MXene-coated Al (lower). Scale bar: 25 mm. (c) Top-view SEM, and (d) corresponding elemental mapping images of MXene-coated Al. Scale bar: 50 μm. The high-resolution XPS spectra of (e) C 1s regions and (f) O 1s regions of MXene and MXene- Al film. (g) XPS spectra of MXene film and MXene-Al film.

2. RESULTS AND DISCUSSION

The passivation film (Al_2O_3) on Al metal (see Figure S2) interferes with the redox reaction on the electrode surface and inhibits the electrochemical activity. The advantages of utilizing the MXene interphase were confirmed through meticulous density functional theory (DFT) calculations. By considering three possible sites on the MXene surface for Al^{3+} adsorption, the MXene-third site was determined to be the most stable site for adsorbing Al^{3+} with an adsorption energy of 4 eV, as illustrated in Figure 1b. In comparison, the Al_2O_3 surface is relatively less intricate, with the O-top site being a possible site for Al^{3+} adsorption with an adsorption energy of 3 eV. The larger adsorption energies of MXene, as compared to Al_2O_3, signify that MXene exhibits a higher affinity toward Al^{3+}.[25] Furthermore, the robust interfacial interactions of Al^{3+} with the MXene surface are evident from the charge density differences depicted in Figure 1c. The diffusion of Al^{3+} was explored by using the climbing-image nudged elastic band (CI-NEB) method. As displayed in Figure 1d,e, the energy barriers of Al^{3+} diffusion on the Al_2O_3 surfaces and MXene were determined to be 1.06 and 0.15 eV, respectively. Consequently, it can be inferred that the heightened adsorption energy of MXene toward Al^{3+} enables the concentration of Al^{3+} preferentially on its surface, while the lower diffusion energy of Al^{3+} facilitates the swift transport of Al^{3+} through the MXene layer. As a result, it can be inferred that the incorporation of the MXene layer is projected to yield improved Al^{3+} adsorption and diffusion properties, along with a stable Al metal anode.

Due to the higher reduction potential of oxygenated functional groups compared to that of Al/Al^{3+}, Al foil can effectively reduce MXene sheets. According to Figure 2a, the Al foil was ionized at the interface of aluminum foil/MXene solution, allowing electrons to transfer easily to the MXene sheets. At the same time, a charge interaction occurred between the resulting Al^{3+} and the O functional group on the surface of the MXene films. This reduction process lowered the electrostatic repulsion contact between the MXene thin films, enabling their self-assembly on surface of metallic aluminum. Upon drying, the Al foil surface uniformly anchored the layered MXene sheet. Compared with the bare Al, the Al surface after MXene treatment changes from silvery white to dark black (Figure 2b). A significant feature of this processing approach is that the treatment process is fast, simple, thermodynamically spontaneous and scalable. The thickness

https://doi.org/10.1021/acsnano.3c07611
ACS Nano 2023, 17, 25027−25036

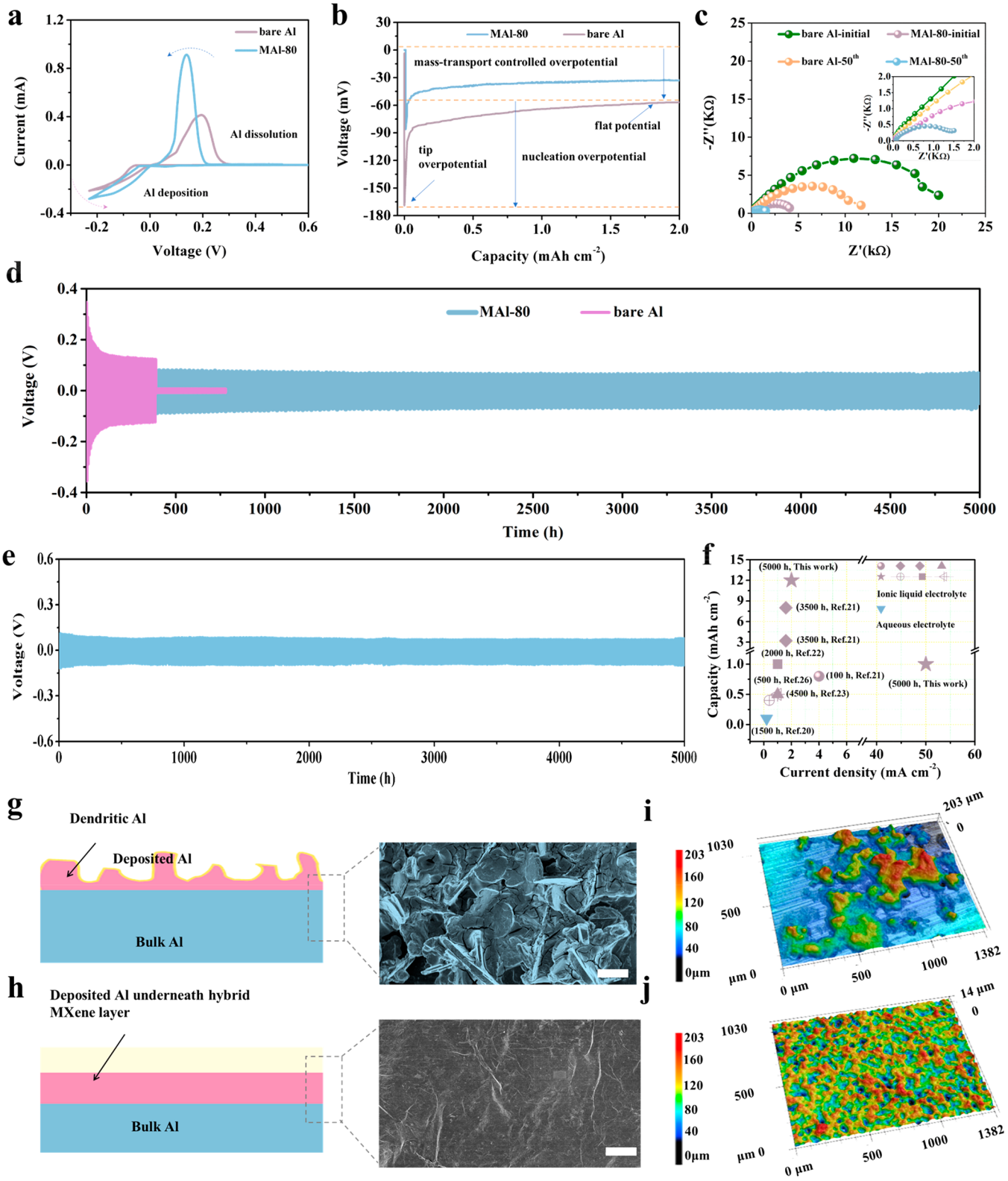

Figure 3. (a) CV curve of Al plating/stripping at 0.1 mV s^{-1}. (b) Voltage hysteresis at current densities of 1 mA cm^{-2}. (c) Nyquist plots of symmetric cells using bare Al and MAl-80 before cycling and after 50 cycles. (d) Comparison of cycling performance of bare Al and MAl-80 at 12 mAh cm^{-2}. (e) Long-term cycling performance of MAl-80 at 50 mA cm^{-2}. (f) Comparison of cycling performance of MAl-80 anode with some previously reported anodes. (g, h) Schematic illustration and SEM images of Al deposition on (g) bare Al and (h) MXene interphase with a plating capacity 5 mA h cm^{-2} at a current density of 10 mA cm^{-2}. Scale bar: 50 mm. (i, j) 3D optical profilometry images of (i) bare Al and (j) MXene interphase with a plating capacity of 5 mA h cm^{-2} at a current density of 10 mA cm^{-2}.

of the MXene coating is positively correlated to the self-assembly reaction time (Figure S3). The MXene modified electrode with different MXene thicknesses is represented as MAl-x (x = 60, 80, and 100 nm, respectively). The optimal

https://doi.org/10.1021/acsnano.3c07611
ACS Nano 2023, 17, 25027−25036

thickness was determined to be 80 nm. Thicker interphase layers were found to have limited Al^{3+} transport, while thinner interphase layers were ineffective in suppressing dendritic growth. Cycling measurements confirmed that the modified Al anode with a moderate thickness (MAl-80) displayed superior cycling stability (see the electrochemical performance section). The scanning electron microscopy (SEM) provides information about the morphological and structural features of the MXene interphase. According to the Figure 2c, Al metal surface evenly covered with MXene layer. Energy dispersive spectroscopy (EDS) mapping shows even distribution of Ti, C, and Al elements (Figure 2d), which is conducive to establishing a uniformly distributed electric field and ion concentration, thereby promoting the uniform diffusion of Al^{3+} in MXene. The conversion of MXene to MAl during the assembly process was proved through X-ray photoelectron spectroscopy (XPS) analysis. The C−O peak (286.4 eV) was weaker in the C 1s XPS spectra, showing the elimination of oxygen-containing groups, while the C−C peak (284.6 eV) was also weakened because C−OH groups were consumed (Figure 2e). The XPS spectra of the O 1s species (Figure 2f) also revealed a reduction in the peak intensity of C−Ti−$(OH)_x$ (532.1 eV) and an increase in the peak intensity of Ti−O (529.5 eV). Compared to pure MXene film, the MAl foil had higher Ti/O (1.56 vs 0.61) and C/O (2.07 vs 1.50) ratios, suggesting that during the spontaneous in situ assembly process, some oxygen-containing functional groups were removed (Figure 2g).[26] These results suggest a strong chemical interaction between MXene and the Al anode. Unlike manual coating, where the obtained coating may fracture and detach during repeated aluminum plating/stripping process, the MXene layer obtained by in situ assembly closely contacts the Al metal, obtaining a uniform surface and better stability.

The electrochemical performance of MAl-*x* was investigated to assess the potential of MXene coating in regulating the deposition behavior of aluminum metal anode. As demonstrated by cyclic voltammetry (CV) measurement, MAl-80 exhibited significantly higher kinetics than bare Al (Figure 3a). Moreover, MAl-80 showed a lower potential for Al plating and stripping compared to bare Al, indicating the effectiveness of the MXene layer in reducing overpotentials. The MAl-80 also displayed higher current intensity, indicating the presence of more effective active sites.[25] As a comparison, the CV curve of the MXene symmetric cell had no significant current peaks (Figure S4). Figure 3b shows the galvanostatic nucleation overpotential voltage profiles at 1 mA cm^{-2}. The results indicate that MAl-80 exhibited a significantly lower nucleation overpotential of only 49 mV, compared to that of bare Al with a nucleation overpotential of 112 mV. This suggests that MAl-80 achieved a reduced nucleation barrier as well as more homogeneous Al nucleation. Moreover, the study performed electrochemical impedance spectroscopy (EIS) prior to and after 50 cycles to comprehend the relationship between Al^{3+} conductivity and the MXene layer in the battery, as shown in Figures 3c and S5. The results demonstrate that the charge transfer resistance of MAl-80 electrode is much lower than that of bare Al, indicating that aluminum ions diffuse rapidly within the MXene layer and its plating/stripping kinetics are enhanced. This is because the MXene coating significantly reduced the interface resistance· at the electrode surface.[27] Notably, according to Figures 3d and S6−S8, MAl-80 exhibited smaller voltage fluctuation than bare Al, suggesting a more reversible Al plating/stripping process due to the presence of the MXene layer. Among MAl-*x*, MAl-80 exhibited a more stable voltage profile with a lower voltage hysteresis of 45 mV over a 5000 h period. In stark contrast, the bare Al-based cell exhibited a voltage dip after only 400 h, leading to cell failure caused by dendrite-induced internal short circuits. Additionally, MAl-60 also exhibits improved cycling stability and lower voltage hysteresis when compared to bare Al. However, MAl-60 displays larger voltage fluctuations after 660 h (Figure S7), likely due to the relatively thin MXene layers being more susceptible to poor mechanical stability as a result of volume fluctuations during the plating/stripping of Al. In addition, it is worth noting that MAl-100 exhibits larger voltage fluctuations and increased polarization, as shown in Figure S8. This is due to the thicker MXene coating, which results in reduced ion transfer between theAl metal and the electrolyte. These results further indicate that MAl-80 would be the optimal protective layer. As shown in Figure 3e, when the current density increases to as high as 50 mA cm^{-2}, the electrode still shows high levels of reversibility and long lifetimes over 5000 h, highlighting the effectiveness of the MXene-coated Al anode in enabling rapid interfacial ion transport and inhibiting the formation of aluminum dendrites. Moreover, the electrochemical performance of the MAl-80@Al asymmetric cell was analyzed. The MAl-80 electrode affords a considerably high CE (99.8%) with stable operations for 600 h under a 2.0 mAh cm^{-2} capacity and a 10.0 mAh cm^{-2} capacity at the current density of 1 mA cm^{-2} (Figure S9a,b), respectively, showing no deterioration trend. Upon cycling under a higher capacity of 5.0 mAh cm^{-2}, the MAl-80 electrode still attains 99.7% at a 1600 cycle (Figure S9c). In addition, the MAl-80 electrode shows almost negligible nucleation overpotentials for Al nucleation and growth (Figure S9d). Figure 3f and Table S1 compare the electrochemical performance of MAl-80 with some previously reported modified Al metal anodes in the literatures.[20−24,28] It can be seen that the electrochemical performance of MAl-80 exhibits significant advances compared with the data reported so far. SEM and surface 3D topography were used to further validate the role of the MXene protective layer in inhibiting dendritic growth. As shown in Figure 3g−j, the deposition of Al metal on the bare Al anode shows irregular and uncontrolled growth, whereas it remains uniform and intact on the MAl-80 anode. The protective effect of the MXene layer was further validated by investigating the morphology of the Al anodes after cycling. As shown in Figure S10, the MAl-80 layer on the surface of the Al anode remains intact and flat after plating, and the dense Al is found to be deposited underneath the MAl-80 layer. These merits of the MXene interphase layer in stabilizing the Al anode were further confirmed in Al-graphite batteries (Figures S11−13). Finally, to further illustrate the excellent properties of the protective layer of the MXene interfacial layer, we explored the surface morphology and elemental distribution of the separators after cycling. As we all know that, due to the chemical instability of polyolefin separators in imidazolium chloride + $AlCl_3$ electrolyte melt, glass fibers are usually chosen as the separators for Al cells. However, early reports in the literature suggest the possibility of a strong chemical affinity between metallic Al and SiO_2, implying that chemical driving forces favor the growth of Al electrodeposits in glass fiber separators. This growth mode was confirmed using SEM and EDS analyses (Figures S14 and S15). It demonstrates that Al has a strong tendency to grow along the glass fibers, generating Al deposits closed attached to the glass fibers. However, as

https://doi.org/10.1021/acsnano.3c07611
ACS Nano 2023, 17, 25027−25036

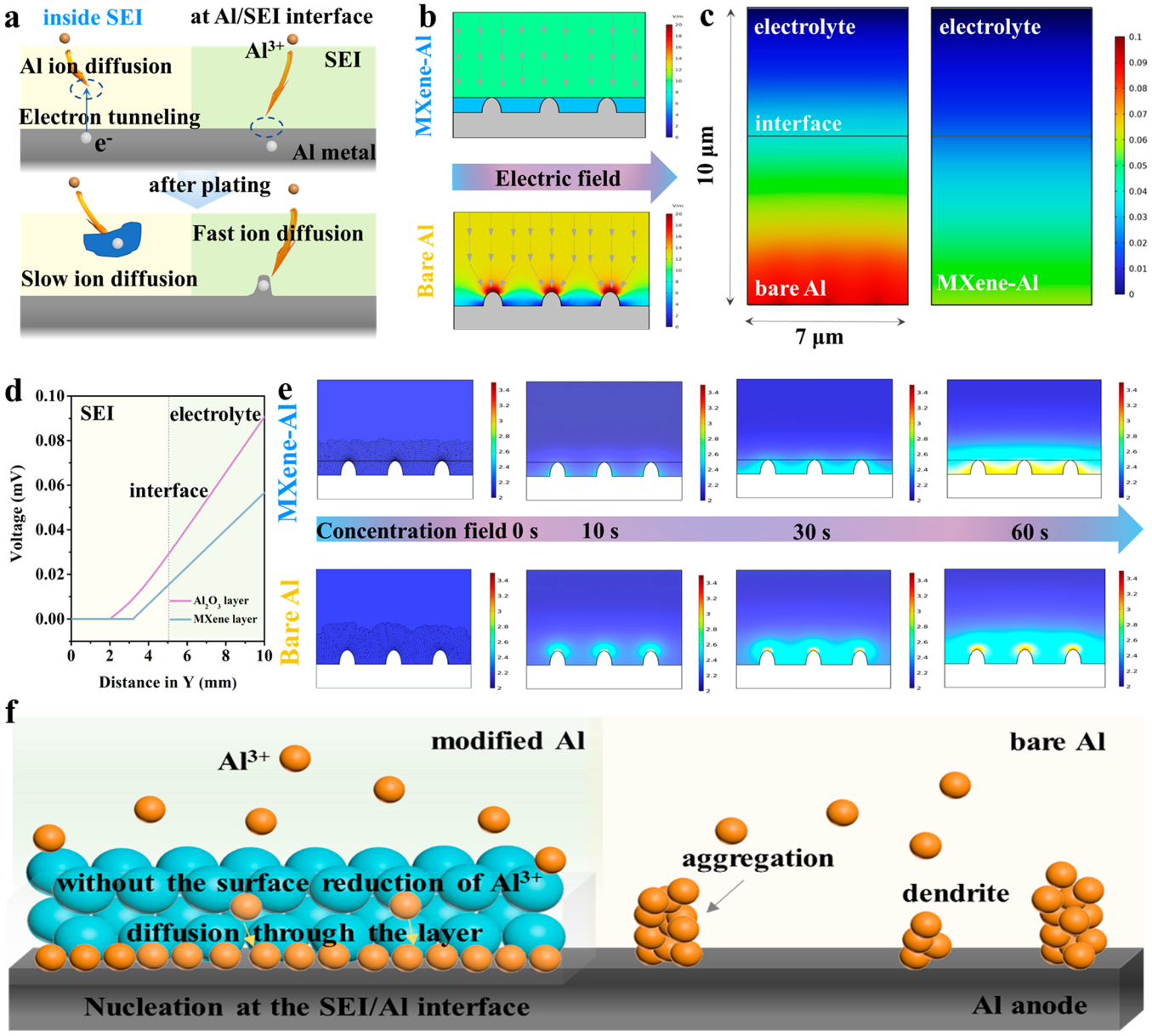

Figure 4. (a) Proposed models of Al nucleation and growth mechanisms after Al plating. (b) Models of the electric field distributions for MAl and bare Al. Finite element simulation of (c) potential and (d) potential distribution for the Al_2O_3 and the MXene layer. (e) Concentration-field simulations reveal the redistribution of Al^{3+} concentration achieved by the MXene protectivelayer. (f) Schematic illustration of Al plating on MAl and bare Al.

shown in Figures S16 and S17, when MAl is used as the negative electrode, there are no apparent Al metal particles deposited on the glass fiber separator. These findings further suggest that metallic aluminum is deposited across MXene at the interface between MXene and Al rather than on the surface of MXene.

Clearly, the MXene protective layer plays a decisive role in regulating the aluminum deposition behavior to obtain excellent electrochemical energy. Figure 4a illustrates that when a fast Al^{3+} diffusion rate is exhibited in the SEI, Al deposition may occur at the SEI/Al interface. A theoretical simulation using COMSOL was performed to clarify the function of the MXene layer in regulating the electric field distribution at the electrode−electrolyte interface (Figure S18). The moderate electronic conductivity of the reduced MXene coating result in a uniform electric field distribution on the aluminum surface, ensuring homogeneous Al^{3+} deposition (Figure 4b). In comparison, at the interface of the bare Al electrode, the electric field distribution shows a distinctive intensity gradient. This gradient creates an area of higher charge, which promotes the nucleation of the Al^{3+} deposition. Due to the tip effect, small protrusions eventually become larger, sharper dendrite tips, which can ultimately lead to cell failure. To better illustrate the Al nucleation and deposition, the distributions of the electric field and Al^{3+} flux were simulated and visualized, as shown in Figure 4c. The MXene layer exhibits a more uniform electric potential field throughout the region. Figure 4d shows a cross-sectional potential profile along the normal Y direction of the MXene layer. The electric potential gradient of the MXene layer is lower than that of the Al_2O_3 layer, which contributes to the reduction of overpotential during cycling.[29] The ion diffusion

https://doi.org/10.1021/acsnano.3c07611
ACS Nano 2023, 17, 25027−25036

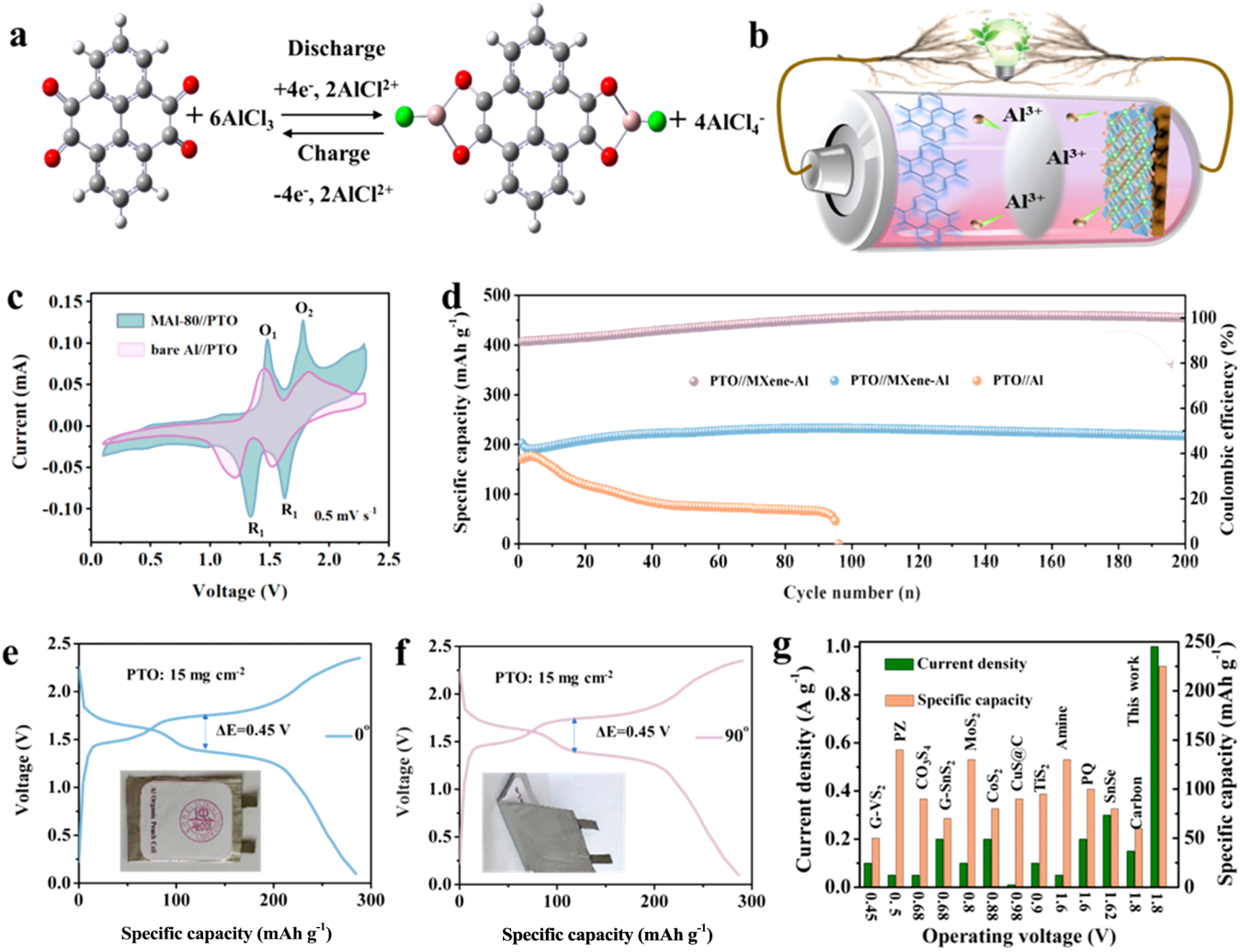

Figure 5. (a) Illustration of the reversible reaction mechanism of the PTO//Al battery. (b) Schematic illustration of PTO//MAl-80 full cell. (c) CV curves at a scan rate of 0.5 mV s^{-1}. (d) Long-term cycling performance at 1 A g^{-1} after 200 cycles. (e, f) Galvanostatic discharge/charge curve of the pouch battery at flat (e) and folded in half (90°) (f) states at 0.1 A g^{-1}. (g) Comparison of operating voltage, capacity versus current densities of the PTO electrode with other electrodes.

process was also investigated by examining the variation of the concentration field with the evolution of the MXene layer (Figure 4e). For a bare Al metal, a significant amount of Al^{3+} rapidly builds up at the protuberances and eventually reaches the maximum concentration values of 3, suggesting a potent driving factor for dendrite formation.[30] The MAl anode, in contrast, exhibits a large concentration of Al^{3+} at the flat surface as opposed to the tips, which can be attributed to the MXene layer achieving a uniform Al^{3+} flux and rapid ion diffusion. Therefore, the evenly distributed Al^{3+} flux and electric field encourage the deposition of dendritic-free aluminum. To summarize, plausible Al deposition scenarios are developed in the artificial hybrid interphase layer, as illustrated in Figure 4f. The fast transport properties of MXene enable fast Al^{3+} diffusion through the MXene film without generating a reduction effect on its surface, resulting in Al deposition at the SEI/Al interface. These processes work together to achieve dendrite-free Al growth beneath the hybrid SEI layer.

The choice of electrode materials for the cathode of Al metal batteries was recently extended to the organic molecule family because sufficient intermolecular space can be utilized to diffuse and store bulky aluminum complex carrier ions due to weak van der Waals intermolecular interactions.[31] Herein, PTO was selected as a model cathode material for assembling Al metal full batteries owing to its high specific capacity and high voltage Al storage characteristics. The reaction scheme of PTO with $AlCl_3$ is shown in Figure 5a. From a chemical structure perspective, PTO can be reduced by accepting up to four electrons, resulting in the formation of a chelate with an $AlCl^{2+}$ ion at each corner of the adjacent carbonyl group. The reversible reaction occurs during the oxidation process. The PTO displays morphology of the nanorod structure (Figure S19). To illustrate the practical application of MXene-Al anodes, PTO cathodes were combined with MAl-80 anode or bare Al foil anode to form a coin-type full cell, respectively (Figure 5b). Based on representative CV curves, two pairs of redox peaks at around 1.76/1.60 V and 1.50/1.30 V are clearly observed (Figure 5c), indicating that the process of ion uptaking is carried out in two steps and the active site is reversible for the redox process.[32] Obviously, compared to the bare PTO//Al battery, the CV curves of PTO//MAl-80 display sharper peak profiles with higher current intensity, suggesting the kinetics advantage of MAl-80 for the conversion

https://doi.org/10.1021/acsnano.3c07611
ACS Nano 2023, 17, 25027−25036

process.[17] As a comparison, the CV curve of the MXene-Al full cell at 0.5 mV s^{-1} has no significant current peaks (Figure S20). As shown in Figure 5d, PTO provides a superior specific capacity of 200 mAh g^{-1} at 1 A g^{-1} and exhibited 100% capacity retention after 200 cycles without significant capacity degradation. However, the PTO//bare Al cell sharply dropped to 20 mAh g^{-1} after 100 cycles. Due to the suppression of Al dendrites during cycling, PTO//MAl-80 cells exhibit superior cycling stability than bare PTO//Al cells. Owing to such fast kinetics, the PTO//MAl-80 batteries deliver superior rate capability. The discharge capacity reaches a decent capacity of 150 mAh g^{-1} even at an high rate of 2 A g^{-1}(Figure S21). Following coin-cell configuration tests, flexible Al-Organic pouch cells with high area PTO loading (15 and 20 mg cm^{-2}) were created to verify the effectiveness of MXene-coated Al metal anode in practice. Various flexibility tests were conducted by subjecting the pouch battery to repetitive bending at different degrees. According to Figure 5e, the galvanostatic discharge/charge curve exhibits a high capacity of 280 mA h g^{-1}, with two flat and long operation voltage of 1.8 and 1.4 V, respectively. This indicates that the PTO electrode undergoes two steps of Redox, consistent with the result of CV curve. Comparing Figures 5e,f and S22, it is evident that there are no discernible polarization issues after folding the flat battery at right angles (90°) and halfway (180°), demonstrating excellent flexibility and robust mechanical properties against repeated bending. Even when the PTO loading was increased to 20 mg cm^{-2}, the battery still exhibited a capacity of 200 mAh g^{-1} at 0.1 A g^{-1} (Figure S23). Electrochemical performances were compared with representative reported RABs such as transition metal chalcogenides,[33] organic positive electrode[34] and carbon paper.[35] The voltage platform, specific capacity, and current density are plotted in Figure 5g. In contrast to the low operating voltage observed in typical transition-metal composite and the low specific capacity observed in typical carbon-based materials, the Al battery system with the PTO electrode exhibits a relatively higher operating voltage platform and higher specific capacity. Considering the potential application in wearable electronic devices, the energy density of the pouch cell was calculated, revealing a maximum energy density of 355 Wh kg^{-1}, comparable to that of lithium-ion batteries (LIBs) (Figure S24 and Table S2).

3. CONCLUSIONS

In summary, we introduce a concept of an emerging in situ MXene film to protect the Al metal anode by a facile spontaneous reaction. This armored MXene is capable to prevent dendrite formation even at high current densities of 50 mA cm^{-2}, resulting in an impressive energy density of 355 Wh kg^{-1} and a long lifespan of 200 cycles in flexible PTO//Al full cells. The excellent electrochemical performance originates from the high ionic conductivity and excellent mechanical flexibility of the MXene film, which ensure stable and efficient operation of the Al-metal anode. This innovative approach to designing a protective layer on the Al-metal anode offers a promising solution for developing safe and high-energy Al-metal-based energy storage systems.

3.1. Methods. *3.1.1. Preparation of $Ti_3C_2T_x$.* First, 20 mL of 9 M HCl (Fisher Scientific) was added to 7.5 mol equiv (2 g) of LiF (Alfa Aesar) and agitated with a Teflon stir bar for 2 min. Next, 2 g of Ti_3AlC_2 powder with a particle size of less than 40 μm were slowly added to the solution over approximately 2 min. The reaction mixture was then gently stirred with a Teflon coated bar rotating at 200 rpm and held at 35 °C for 24 h to ensure a complete reaction. Afterward, the mixture was meticulously washed several times with deionized water and centrifuged at 8000 rpm to isolate the desired product. The pH of the supernatant was carefully monitored and found to be >6 after the last centrifugation. Finally, the $Ti_3C_2T_x$ solution was obtained through ultrasound and centrifugation

3.1.2. Preparation of MXene-Al Anodes. The $Ti_3C_2T_x$ dispersion of 10 mg mL^{-1} was diluted with deionized water to 0.5 mg mL^{-1}. Then the Al sheet was floated on the surface of the prepared $Ti_3C_2T_x$ dispersion, and these $Ti_3C_2T_x$ sheets were reduced at different times to form an reduced $Ti_3C_2T_x$ layer on the surface of the metal Al. After that, the Al foil with $Ti_3C_2T_x$ films was washed with deionized water and vacuum-dried to obtain the MXene-Al anode.

3.1.3. Preparation of Ionic Liquid Electrolytes. 1-Ethyl-3-methylimidazolium chloride [EMIm]Cl and anhydrous aluminum chloride ($AlCl_3$) were mixed with 1.3 mol equivalent and continuously stirred in an Ar atmosphere Glovebox ($[O_2]$ < 0.1 ppm, $[H_2O]$ < 0.1 ppm). The obtained light-yellow electrolyte was held in the glovebox for 12 h for standby.

3.1.4. Assembly of Al//Al Symmetric Cells and Al//PTO Batteries. The coin symmetric batteries were assembled with identical electrodes of bare Al or MAl-*x*, as-prepared ionic liquid electrolytes (≤10 ppm of water) as the electrolyte, and glass fiber separators. To assemble Al//PTO pouch-shaped cells, the cathode was prepared by mixing PTO powder, Ketjen black, and PTFE in a weight ratio of 6:3:1 in isopropanol (≥99.7%, Sigma-Aldrich) solvent. Then, the slurry was rolled into an active material membrane and dried at 120 °C for 12 h. Based on such cathodes (PTO mass loading: 15 mg cm^{-2}), Al//PTO pouch-shaped cells were assembled by using bare Al or MAl-80 as anodes, as−prepared ionic liquid electrolytes as electrolyte and glass fiber as separators. For the belt-shaped battery, PTO membrane and Al foil were cut in sizes of 2 cm × 5 cm, respectively. The pouch-shaped PTO//Al battery was obtained through a vacuum sealed process after adding as-prepared ionic liquid as electrolyte. All batteries were assembled in an Ar-filled glovebox and aged for 12 h before performed electrochemical measurements.

3.1.5. Materials Characterizations. Scanning electron microscopy (JEOL JSM-7500F and Phenom XL) is used to characterize the morphology of the sample. XPS (PerkinElmer PHI 1600 ESCA) was used to characterize the chemical composition of MXeneand MXene-Al samples.

3.1.6. Electrochemical Measurements. Cyclic voltammetry (CV) curves were conducted on an electrochemical workstation (CHI 604E). Galvanostatic cycling tests were also carried out by a LAND battery test system (Wuhan, China). Electrochemical impedance spectroscopy (EIS) measurements were performed on the CHI 604E electrochemical workstation with an amplitude of 5 mV in a frequency ranging from 100 kHz to 1 mHz.

3.1.7. Density Functional Theory Calculations. State-of-the-art calculations using density functional theory (DFT) were performed to investigate the properties of the system. The calculations utilized the projector-augmented wave (PAW) method, as implemented in the Vienna ab initio simulation package (VASP). The exchange-correlation interaction was described using a generalized gradient approximation (GGA) of the Perdew−Burke−Ernzerhof (PBE)

https://doi.org/10.1021/acsnano.3c07611
ACS Nano 2023, 17, 25027−25036

functional, while the van der Waals (vdW) correction DFT-D3 proposed by Grimme was used to describe the dispersion interaction. To ensure accurate results, a 4 × 4 × 1 supercell with 20 Å vacuum was employed, and an energy cutoff of 500 eV with a Gamma-centered 3 × 3 × 1 *k*-points mesh was used for all calculations. The structures were relaxed until the forces and total energy on all atoms had converged to less than 0.05 eV $Å^{-1}$ and 1 × 10^{-5} eV.

3.1.8. Simulation of the Electric Field Contribution in COMSOL. The length of the two electrodes and the distance between the two electrodes are 10 μm, respectively. The ionic conductivity of the ionic liquid electrolytes was 13.5 S m^{-1} and the electrical conductivity of MXene and Al metal were 7.1 × 10^3 and 1.67 × 10^7 S m^{-1}, respectively.

ASSOCIATED CONTENT

Supporting Information

The Supporting Information is available free of charge at https://pubs.acs.org/doi/10.1021/acsnano.3c07611.

More sample characterizations including surface structure, electrochemical property, and battery performance (PDF)

AUTHOR INFORMATION

Corresponding Author

Xuebin Yu − *Department of Materials Science, Fudan University, Shanghai 200433, China;* orcid.org/0000-0002-4035-0991; Email: yuxuebin@fudan.edu.cn

Authors

Long Yao − *Department of Materials Science, Fudan University, Shanghai 200433, China; Institute of Energy Materials Science, University of Shanghai for Science and Technology, Shanghai 200093, China*

Shunlong Ju − *Department of Materials Science, Fudan University, Shanghai 200433, China*

Tian Xu − *Department of Materials Science, Fudan University, Shanghai 200433, China*

Wenbin Wang − *Department of Materials Science, Fudan University, Shanghai 200433, China*

Complete contact information is available at: https://pubs.acs.org/10.1021/acsnano.3c07611

Notes

The authors declare no competing financial interest.

ACKNOWLEDGMENTS

This work was partially supported by the National Natural Science Foundation of China (51971065) and the Innovation Program of Shanghai Municipal Education Commission (2019-01-07-00-07-E00028).

REFERENCES

(1) Fang, R.; Xu, J.; Wang, D. W. Covalent Fixing of Sulfur in Metal−Sulfur Batteries. *Energy Environ. Sci.* **2020**, *13*, 432−471.

(2) Li, M.; Lu, J.; Ji, X.; Li, Y.; Shao, Y.; Chen, Z.; Zhong, C.; Amine, K. Design Strategies for Nonaqueous Multivalent-Ion and Monovalent-Ion Battery Anodes. *Nat. Rev. Mater.* **2020**, *5*, 276−294.

(3) Pan, Z.; Liu, Xi; Yang, J.; Li, X.; Liu, Z.; Loh, X. J.; Wang, J. Aqueous Rechargeable Multivalent Metal-Ion Batteries: Advances and Challenges. *Adv. Energy Mater.* **2021**, *11*, 2100608.

(4) Yoo, D.; Heeney, M.; Glöcklhofer, F.; Choi, J. W. Tetradiketone Macrocycle for Divalent Aluminium Ion Batteries. *Nat. Commun.* **2021**, *12*, 2386.

(5) Wang, H.; Zhao, L.; Zhang, H.; Liu, Y.; Yang, L.; Li, F.; Liu, W.; Dong, X.; Li, X.; Li, Z.; Qi, X.; Wu, L.; Xu, Y.; Wang, Y.; Wang, K.; Li, Q.; Yan, S.; Zhang, X.; Li, F.; Yang, H.; Li, H. Revealing the Multiple Cathodic and Anodic Involved Charge Storage Mechanism in an $FeSe_2$ Cathode for Aluminium-Ion Batteries by *in Situ* Magnetometry. *Energy Environ. Sci.* **2022**, *15*, 311−319.

(6) Jiang, M.; Fu, C.; Meng, P.; Ren, J.; Wang, J.; Bu, J.; Dong, A.; Zhang, J.; Xiao, W.; Sun, B. Challenges and Strategies of Low-Cost Aluminum Anodes for High-Performance Al-Based Batteries. *Adv. Mater.* **2022**, *34*, 2102026.

(7) Qi, Y.; Li, Q. J.; Wu, Y.; Bao, S.; Li, C.; Chen, Y.; Wang, G.; Xu, M. A Fe_3N/Carbon Composite Electrocatalyst for Effective Polysulfides Regulation in Room Temperature Na-S Batteries. *Nat. Commun.* **2021**, *12*, 6347.

(8) Li, S.; Zhu, H.; Liu, Y.; Han, Z.; Peng, L.; Li, S.; Yu, C.; Cheng, S.; Xie, J. Codoped Corous Carbon Nanofibres as a Potassium Metal Host for Nonaqueous K-Ion Batteries. *Nat. Commun.* **2022**, *13*, 4911.

(9) Chen, Z.; Yang, Q.; Wang, D.; Chen, A.; Li, X.; Huang, Z.; Liang, G.; Wang, Y.; Zhi, C. A High-Performance Cathode for Magnesium Ion Batteries Based on a Conversion Mechanism. *ACS Nano* **2022**, *16* (4), 5349−5357.

(10) Wang, W.; Huang, G.; Wang, Y.; Cao, Z.; Cavallo, L.; Hedhili, M. N.; Alshareef, H. N. Organic Acid Etching Strategy for Dendrite Suppression in Aqueous Zinc-Ion Batteries. *Adv. Energy Mater.* **2022**, *12*, 2102797.

(11) Pang, Q.; Meng, J.; Gupta, S.; Hong, X.; Kwok, C. Y.; Zhao, J.; Jin, Y.; Xu, L.; Karahan, O.; Wang, Z.; Toll, S.; Mai, L.; Nazar, L. F.; Balasubramanian, M.; Narayanan, B.; Sadoway, D. R. Fast-Charging Aluminium−Chalcogen Batteries Resistant to Dendritic Shorting. *Nature* **2022**, *608*, 704−711.

(12) Hou, S.; Ji, X.; Gaskell, K.; Wang, P.; Wang, L.; Xu, J.; Sun, R.; Borodin, O.; Wang, C. Solvation Sheath Reorganization Enables Divalent Metal Batteries with Fast Interfacial Charge Transfer Kinetics. *Science* **2021**, *374*, 172−178.

(13) Wang, G.; Dmitrieva, E.; Kohn, B.; Scheler, U.; Liu, Y.; Tkachova, V.; Yang, L.; Fu, Y.; Ma, Ji; Zhang, P.; et al. An Efficient Rechargeable Aluminium−Amine Battery Working Under Quaternization Chemistry. *Angew. Chem., Int. Ed.* **2022**, *61*, No. e202116194.

(14) Tu, J.; Song, W.; Lei, H.; Yu, Z.; Chen, L.; Wang, M.; Jiao, S. Nonaqueous Rechargeable Aluminum Batteries: Progresses, Challenges, and Perspectives. *Chem. Rev.* **2021**, *121*, 4903−4961.

(15) Meng, P.; Huang, J.; Yang, Z.; Wang, F.; Lv, T.; Zhang, J.; Fu, C.; Xiao, W. A Low-Cost and Air-Stable Rechargeable Aluminum-Ion Battery. *Adv. Mater.* **2022**, *34*, 21065.

(16) Yan, C.; Lv, C.; Jia, B.; Zhong, L.; Cao, X.; Guo, X.; Liu, H.; Xu, W.; Liu, D.; Yang, L.; Liu, J.; Hng, H. H.; Chen, W.; Song, L.; Li, S.; Liu, Z.; Yan, Q.; Yu, G. Reversible Al Metal Anodes Enabled by Amorphization for Aqueous Aluminum Batteries. *J. Am. Chem. Soc.* **2022**, *144* (25), 11444−11455.

(17) Yan, C.; Lv, C.; Wang, L.; Cui, W.; Zhang, L.; Dinh, K. N.; Tan, H.; Wu, C.; Wu, T.; Ren, Y.; Chen, J.; Liu, Z.; Srinivasan, M.; Rui, X.; Yan, Q.; Yu, G. Architecting a Stable High-Energy Aqueous Al-Ion Battery. *J. Am. Chem. Soc.* **2020**, *142*, 15295−15304.

(18) Ran, Q.; Shi, H.; Meng, H.; Zeng, S.; Wan, W.; Zhang, W.; Wen, Z.; Lang, X.; Jiang, Q. Aluminum-Copper Alloy Anode Materials for High-Energy Aqueous Aluminum Batteries. *Nat. Commun.* **2022**, *13*, 576.

(19) Lin, M.; Gong, M.; Lu, B.; Wu, Y.; Wang, D.; Guan, M.; Angell, M.; Chen, C.; Yang, J.; Hwang, B.; Dai, H. An Ultrafast Rechargeable Aluminium-Ion Battery. *Nature* **2015**, *520*, 324.

(20) Long, Y.; Li, H.; Ye, M.; Chen, Z.; Wang, Z.; Tao, Y.; Weng, Z.; Qiao, S.; Yang, Q. Suppressing Al Dendrite Growth towards a Long-Life Al-Metal Battery. *Energy Storage Mater.* **2021**, *34*, 194−202.

(21) Zheng, J.; Bock, D. C.; Tang, T.; Zhao, Q.; Yin, J.; Tallman, K. R.; Wheeler, G.; Liu, X.; Deng, Y.; Jin, S.; Marschilok, A. C.; Takeuchi, E. S.; Takeuchi, K. J.; Archer, L. A. Regulating

Electrodeposition Morphology in High-Capacity Aluminium and Zinc Battery Anodes Using Interfacial Metal−Substrate Bonding. *Nat. Energy* **2021**, *6*, 398−406.
(22) Heo, Y. H.; Lee, J.; Ha, S.; Chan Hyun, J.; Kang, D. H.; Yoon, J.; Kim, H. S.; Choi, Y.; Chan Kang, Y.; Jin, H.-J.; et al. 3D-structured bifunctional MXene paper electrodes for protection and activation of Al metal anodes. *J. Mater. Chem. A* **2023**, *11*, 14380−14389.
(23) Meng, Y.; Wang, J.; Wang, M.; Peng, Q.; Xie, Z.; Zhu, Z.; Liu, Z.; Wang, W.; Zhang, K.; Liu, H.; et al. Anode-Free Aluminum Electrode with Ultralong Cycle Life and High Coulombic Efficiency Exceeding 99.92% Enabled by a Lattice-Matching Layer. *Adv. Energy Mater.* **2023**, *13*, 2301322.
(24) He, S.; Wang, J.; Zhang, X.; Chu, W.; Zhao, S.; He, D.; Zhu, M.; Yu, H. Aluminum Dendrite Suppression by Graphite Coated Anodes of Al-metal Batteries. *J. Mater. Chem. A* **2023**, *11*, 17020−17026.
(25) Li, X.; Li, M.; Luo, K.; Hou, Y.; Li, P.; Yang, Q.; Huang, Z.; Liang, G.; Chen, Z.; Du, S.; Huang, Q.; Zhi, C. Lattice Matching and Halogen Regulation for Synergistically Induced Uniform Zinc Electrodeposition by Halogenated Ti_3C_2 MXenes. *ACS Nano* **2022**, *16*, 813.
(26) Shekhirev, M.; Shuck, C. E.; Sarycheva, A.; Gogotsi, Y. Characterization of MXenes at Every Step, from Their Precursors to Single Flakes and Assembled Films. *Prog. Mater. Sci.* **2021**, *120*, 100757.
(27) Wu, F.; Zhu, N.; Bai, Y.; Gao, Y.; Wu, C. An Interface-Reconstruction Effect for Rechargeable Aluminum Battery in Ionic Liquid Electrolyte to Enhance Cycling Performances. *Green Energy Environ.* **2018**, *3*, 71−77.
(28) Meng, Y.; Wang, M.; Li, K.; Zhu, Z.; Liu, Z.; Jiang, T.; Zheng, X.; Zhang, K.; Wang, W.; Peng, Q.; Xie, Z.; Wang, Y.; Chen, W. Reversible, Dendrite-Free, High-Capacity Aluminum Metal Anode Enabled by Aluminophilic Interface Layer. *Nano Lett.* **2023**, *23*, 2295−2303.
(29) Hu, A.; Chen, W.; Du, X.; Hu, Y.; Lei, T.; Wang, H.; Xue, L.; Li, Y.; Sun, H.; Yan, Y.; et al. An Artificial Hybrid Interphase for an Ultrahigh-Rate and Practical Lithium Metal Anode. *Energy Environ. Sci.* **2021**, *14*, 4115.
(30) Zhao, M.; Lv, Y.; Zhao, S.; Xiao, Y.; Niu, J.; Yang, Q.; Qiu, J.; Wang, F.; Chen, S. Simultaneously Stabilizing Both Electrodes and Electrolytes by a Self-Separating Organometallics Interface for High Performance Zinc-Ion Batteries at Wide Temperatures. *Adv. Mater.* **2022**, *34*, 2206239.
(31) Walter, M.; Kravchyk, K. V.; Böfer, C.; Widmer, R.; Kovalenko, M. V. Polypyrenes as High-Performance Cathode Materials for Aluminum Batteries. *Adv. Mater.* **2018**, *30*, 1705644.
(32) Yang, H.; Xu, R.; Yao, Y.; Ye, S.; Zhou, X.; Yu, Y. Multicore−Shell Bi@N-doped Carbon Nanospheres for High Power Density and Long Cycle Life Sodium- and Potassium-Ion Anodes. *Adv. Funct. Mater.* **2019**, *29*, 1809195.
(33) (a) Hu, Y.; Luo, B.; Ye, D.; Zhu, X.; Lyu, M.; Wang, L. An Innovative Freeze-Dried Reduced Graphene Oxide Supported SnS_2 Cathode Active Material for Aluminum-Ion Batteries. *Adv. Mater.* **2017**, *29*, 1606. (b) Li, H.; Yang, H.; Sun, Z.; Shi, Y.; Cheng, H. M.; Li, F. A Highly Reversible Co_3S_4 Microsphere Cathode Material for Aluminum-Ion Batteries. *Nano Energy* **2019**, *56*, 100. (c) Wang, S.; Jiao, S.; Wang, J.; Chen, H. S.; Tian, D.; Lei, H.; Fang, D. N. High-Performance Aluminum-Ion Battery with CuS@C Microsphere Composite Cathode. *ACS Nano* **2017**, *11*, 469−477. (d) Wu, L.; Sun, R.; Xiong, F.; Pei, C.; Han, K.; Peng, C.; Fan, Y.; Yang, W.; An, Q.; Mai, L. A Rechargeable Aluminum-Ion Battery based on a VS_2 Nanosheet Cathode. *Phys. Chem. Chem. Phys.* **2018**, *20*, 22563−22568. (e) Yang, W.; Lu, H.; Cao, Y.; Xu, B.; Deng, Y.; Cai, W. Flexible Free-Standing MoS_2/Carbon Nanofibers Composite Cathode for Rechargeable Aluminum-Ion Batteries. ACS Sustainable. *Chem. Eng.* **2019**, *7*, 4861−4867. (f) Zhuang, R.; Huang, Z.; Wang, S.; Qiao, J.; Wu, J. C.; Yang, J. Binder-Free Cobalt Sulfide@Carbon Nanofibers Composite Films as Cathode for Rechargeable Aluminum-Ion Batteries. *Chem. Eng. J.* **2021**, *409*, 128235. (g) Geng, L.; Scheifers, J. P.; Fu, C.; Zhang, J.; Fokwa, B. P. T.; Guo, J. Titanium Sulfides as Intercalation-Type Cathode Materials for Rechargeable Aluminum Batteries. *ACS Appl. Mater. Interfaces* **2017**, *9*, 21251−21257. (h) Zhang, Y.; Zhang, B.; Li, J.; Liu, J.; Huo, X.; Kang, F. SnSe Nano-Particles as Advanced Positive Electrode Materials for Rechargeable Aluminum-Ion Batteries. *Chem. Eng. J.* **2021**, *403*, 126377.
(34) (a) Chen, J.; Zhu, Q.; Jiang, L.; Liu, R.; Yang, Y.; Tang, M.; Wang, J.; Wang, H.; Guo, L. Rechargeable Aqueous Aluminum Organic Batteries. *Angew. Chem., Int. Ed.* **2021**, *60*, 5794−5799. (b) Wang, G.; Dmitrieva, E.; Kohn, B.; Scheler, U.; Liu, Y.; Tkachova, V.; Yang, L.; Fu, Y.; Ma, J.; Zhang, P.; et al. An Efficient Rechargeable Aluminium−Amine Battery Working Under Quaternization Chemistry. *Angew. Chem., Int. Ed.* **2022**, *61*, No. e202116194. (c) Kim, D. J.; Yoo, D. J.; Otley, M. T.; Prokofjevs, A.; Owczarek, M.; Lee, S. J.; Choi, J. W.; Stoddart, J. F.; Pezzato, C. Rechargeable Aluminium Organic Batteries. *Nat. Energy* **2019**, *4*, 51−59.
(35) Sun, H.; Wang, W.; Yu, Z.; Yuan, Y.; Wang, S.; Jiao, S. A new Aluminium-Ion Battery with High Voltage, High Safety and Low Cost. *Chem. Commun.* **2015**, *51*, 11892−11895.

https://doi.org/10.1021/acsnano.3c07611
ACS Nano 2023, 17, 25027−25036